

---

# CAMIL: CONTEXT-AWARE MULTIPLE INSTANCE LEARNING FOR WHOLE SLIDE IMAGE CLASSIFICATION

---

**Olga Fourkioti**

Cancer Biology  
The Institute of Cancer Research  
London, United Kingdom  
olga.fourkioti@icr.ac.uk

**Avi Arampatzis**

Department of Electrical & Computer Engineering  
Democritus University of Thrace  
Xathi, Greece

**Chen Jin**

Centre for Medical Imaging  
University College London  
London, United Kingdom

**Mat De Vries**

Cancer Biology  
The Institute of Cancer Research  
London, United Kingdom

**Daniel Alexander**

Centre for Medical Imaging  
University College London  
London, United Kingdom

**Chris Bakal**

Cancer Biology  
The Institute of Cancer Research  
London, United Kingdom  
chris.bakal@icr.ac.uk

## ABSTRACT

Cancer diagnoses typically involve human pathologists examining whole slide images (WSIs) of tissue section biopsies to identify tumor cells and their subtypes. However, artificial intelligence (AI)-based models, particularly weakly supervised approaches, have recently emerged as viable alternatives. Weakly supervised approaches often use image subsections or tiles as input, with the overall classification of the WSI based on attention scores assigned to each tile. However, this method overlooks the potential for false positives/negatives because tumors can be heterogeneous, with cancer and normal cells growing in patterns larger than a single tile. Such errors at the tile level could lead to misclassification at the tumor level. To address this limitation, we developed a novel deep learning pooling operator called CHARM (Contrastive Histopathology Attention Resolved Models). CHARM leverages the dependencies among single tiles within a WSI and imposes contextual constraints as prior knowledge to multiple instance learning models. We tested CHARM on the subtyping of non-small cell lung cancer (NSLC) and lymph node (LN) metastasis, and the results demonstrated its superiority over other state-of-the-art weakly supervised classification algorithms. Furthermore, CHARM facilitates interpretability by visualizing regions of attention.

**Keywords** Cancer · Histopathology · Multiple Instance Learning · Weakly-supervised Learning · Attention Model

## 1 Introduction

Visual analysis of tissue biopsy sections (Whole Slide Images; WSIs) provides a wealth of phenotypic information and is the foundation of cancer pathology [1]. In recent years, deep learning (DL) methods have revolutionized the development of highly accurate diagnostic machines [2] whose performance on cancer classification and diagnosis tasks can match or even exceed that of trained experts. [3–8]. However, developing efficient deep neural network (DNN) models for cancer pathology has often required meticulous pixel-level annotations of every WSI with expert-based ground-truth descriptions [6]. Training DNN classification models in a weakly-supervised setting using only slide-level

labels has demonstrated exceptional classification accuracy on test data, laying the foundation for the deployment of scalable computational decision support systems in clinical practice [9–12].

Notably, in the context of cancer histopathology WSIs are not processed as a single image by DNN models. Instead, WSIs are frequently subdivided into smaller ‘tiles’, which are used for input. The task is then to classify the whole WSI (and tumor) based on DL features measured in individual tiles. Most current methods for weakly supervised WSI classification use the Multiple Instance Learning (MIL) framework, which considers each WSI as a ‘bag’ of tiles and attempts to learn the slide-level label.

A major bottleneck in the deployment of MIL models, and the weakly-supervised learning paradigm in general, is that the MIL model is permutation invariant, meaning that the tiles within a WSI exhibit no ordering among each other [13, 14]. In other words, the spatial relationship of one tile to another is unknown, or dependencies between tiles are learned implicitly by neural modules such as transformers [15], graph neural networks [16], or recurrent neural networks [17].

Considering a tile’s spatial location in the WSI is particularly relevant in cancer histopathology, where cancer and normal cells are not necessarily distributed randomly inside an image. For example, there can be underlying biological patterns governing their spatial arrangement. Therefore, failing to inject the biological pattern as a prior can potentially generate false positives. For example, a tile classified as cancerous based on cells within the tile may actually be non-cancerous if considered in its environmental context (false positive) - or vice-versa (false negative). Both types of errors propagate to misdiagnosis on the WSI level. Importantly, unlike other types of relationships (i.e. between words in a sentence), in the context of cancer histopathology, the positional embeddings are very difficult to learn because tumor tissues can exhibit complex, heterogeneous, and often poorly predictable architectures.

We propose a new framework called Context-Aware Multiple Instance Learning (CAMIL), which leverages contextual information from neighboring tiles to enhance the classification of a single tile. Our approach aims to impose prior knowledge on the MIL model, reducing training ambiguity and boosting performance. We formulate this neighborhood prior as a matrix that indicates whether pairs of patches are spatially adjacent. This matrix operates as a mask that enables us to attend only to each patch and its neighbors, generate a neighborhood descriptor of every tile’s closest neighbors, calculate their attention coefficients, and produce an average attention score for each tile inside a WSI. By encouraging similar attention weights between instances that share similar feature representations, CAMIL mitigates the risk of incorrectly classifying isolated or noisy instances. Furthermore, the attention weights increase the model’s interpretability by providing insights into sub-regions of high diagnostic value within a WSI. Our code is available on GitHub.<sup>1</sup>

## 2 Related work

Typically, to serve as input for a DNN, a WSI is divided into non-overlapping fixed-size tiles, which are assigned a weak label based on the slide-level diagnosis. Under the MIL formulation, the prediction of a WSI label (i.e. cancer yes/no, cancer type) can come either directly from the tile predictions [11, 17–19], or from a higher-level bag representation resulting from the aggregation of the tile features [13, 20–22]. The former approach is referred to as instance based. The latter, known as the bag embedding-based approach [13, 22], has empirically demonstrated superior performance. Most recent bag embedding-based approaches employ attention mechanisms [23], which assign an attention score to every tile reflecting its relative contribution to the collective WSI-level representation. Attention scores enable the automatic localisation of sub-regions of high diagnostic value in addition to informing the WSI-level label [21, 24, 25].

Attention-based MIL models vary in how they explore tissue structure in WSIs. Many are permutation invariant, meaning they assume the tiles are independent and identically distributed. Building upon this assumption, a recent study [20] proposed a learnable attention-based MIL pooling operator which computes the bag embedding as the average of all tile features in the WSI weighted by their respective attention score. This operator has been widely adopted and modified with the addition of a clustering layer [21, 26, 27] to further encourage the learning of semantically-rich, separable class-specific features. Furthermore, using ‘pseudo bags’ [28], the original bag (WSI) can be split into several smaller bags to alleviate the issue of the limited number of training data.

However, permutation invariant operators cannot inherently capture the structural dependencies among different tiles at the input. The lack of bio-topological information has partially been remedied by the introduction of feature similarity scores instead of positional encodings to model the mutual tile dependencies within a WSI [14, 29, 30]. For instance, DSMIL [31] utilizes a non-local operator to compute an attention score for each tile by measuring its feature representation against that of a critical tile. Recently, to consider the correlations between the different tiles of a WSI, transformer-based architectures have been introduced, which usually make use of a learnable position-dependent

<sup>1</sup><https://github.com/olgafour1/CAMIL.git>



signal to incorporate the spatial information of the image [16, 32]. For instance, TransMIL [15] is a transformer-like architecture trained end-to-end to optimize for the classification task and produce attention scores while simultaneously learning the positional embeddings. However, transformer-based approaches may miss the underlying biological patterns governing the slide’s spatial arrangement.

In CAMIL, we provide explicit guidance information regarding the neighbors of every tile as we argue that they can provide a valuable rich source of information. To this end, we propose a neural network architecture which leverages the dependencies between neighboring tiles of a WSI by enforcing bio-topological constraints to enhance performance effectively. Unlike most existing MIL approaches where the relationships developed between neighboring tiles are omitted, in our approach, the neighborhood of every tile conveys additional information about the structure of a WSI.

### 3 Methodology

CAMIL is based on the intuition that the neighborhood of each tile provides information regarding the extent of attention given to each tile by the model. Drawing an analogy between our framework and how a pathologist examines a biopsy slide, one could think of zooming in and out of a specific sub-region as a way to thoroughly inspect its wider neighborhood to understand the surrounding microenvironment and tissue context better.

In CAMIL, we re-adjust each tile’s individual attention score by aggregating the attention scores of its neighborhood. For example, tiles with high attention scores that are surrounded by other high-scoring tiles should be recognized as important. Conversely, the presence of a tile classified by the model as important in a low-scoring neighborhood could be, in some cases, attributed to noise, and this should be reflected in its final attention score.

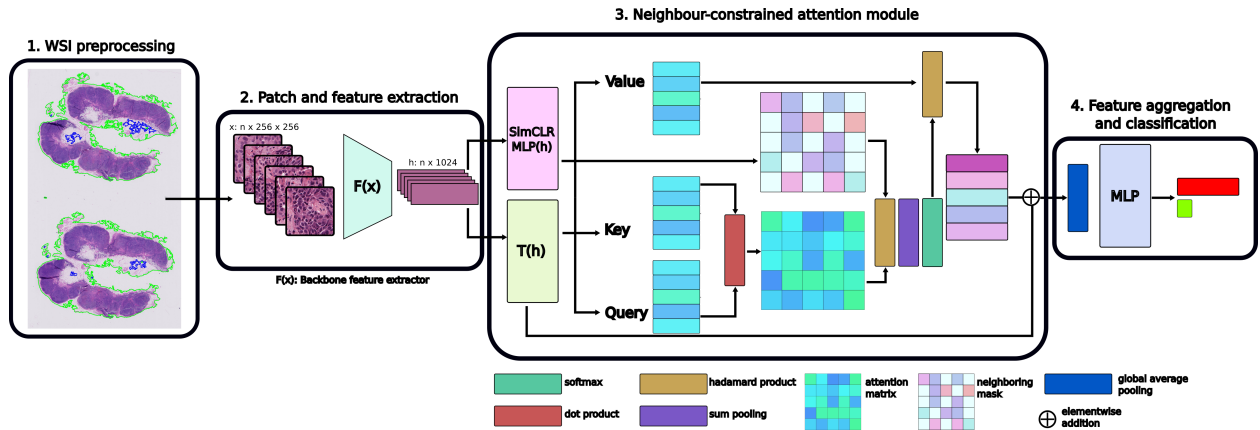


Figure 1: An overview of the CAMIL model architecture. First, WSIs are preprocessed to separate tissue from the background. Then the WSIs are split into fixed-size tiles of size  $256 \times 256$  and fed through a pre-trained feature extractor to obtain feature representations of size 1024 for each tile. The tile feature representations are then used as input to our neighbor-constrained attention module. This module allows attending over each patch and its neighboring patches, generating a neighborhood descriptor of each tile’s closest neighbors, and calculating their attention coefficients. The output layer then aggregates the tile-level attention scores produced in the previous layer to emit a final slide classification score.

The overview of CAMIL can be seen in Fig. 1. It can be decomposed into four elements:

1. A WSI-preprocessing phase automatically segments the tissue region of each WSI and divides it into many smaller patches (e.g.  $256 \times 256$  pixels).
2. A patch and feature extraction module, consisting of a stack of convolutional, max pooling and linear layers responsible for transforming the original tile input to low dimensional feature representations:  $H = \{h_1, \dots, h_i, \dots, h_N\}$ ,  $h_i \in \mathbb{R}^{n \times d}$ , where  $d$  is the embedding dimensions of a tile,  $n$  the number of tiles within a WSI ( $n$  differs among different WSIs), and  $N$  the number of WSIs.
3. An neighbor-constrained attention mechanism with a contrastive learning block that encapsulates the neighborhood prior responsible for outputting an attention vector of size  $N \times 1$ .
4. A feature aggregator and classification layer that aggregates the tile-level attention scores produced in the previous layer and produces a slide-level prediction.

### 3.1 Feature extractor

To encourage similar attention weights between instances that share similar feature representations, we propose using self-supervised contrastive learning. Specifically, we consider SimCLR [33], one of the most popular self-supervised learning frameworks that enables semantically rich feature representations to be learned by minimizing the distance between different augmented versions of the same image data.

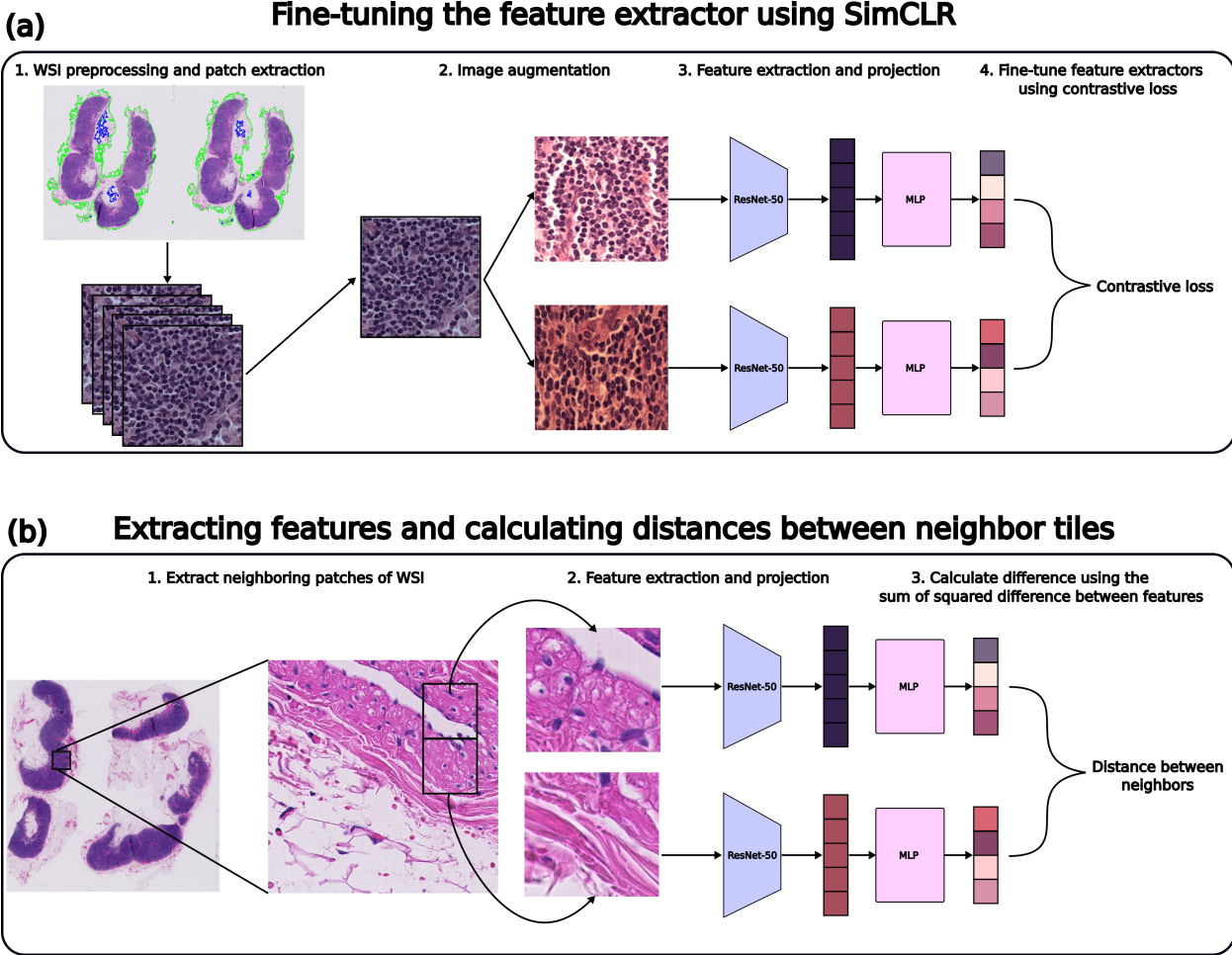


Figure 2: The training and inference steps of SimCLR. During training, two different augmentations are done on the same tile. These two augmentations are chosen from four possible augmentations (color distortion, zoom, rotation, and reflection) using a stochastic data augmentation module. These two augmentations of the same tile are fed through a ResNet-50 pre-trained on ImageNet with an additional projection head. The final convolutional block of ResNet-50 and the projection head are then fine-tuned by minimizing the contrastive loss (temperature-scaled cross entropy) between the two tiles. During inference, features are extracted from the fine-tuned ResNet-50. Distances between neighboring patches are calculated and used in the following neighbor-constrained attention module.

Following the dividing of the segmented tissue region into tiles, we use two differentially augmented versions of the same tile as an input to an instance-level feature encoder  $F(x)$ , implemented as a ResNet-50. In CAMIL, this is followed by a projection head, which is a multi-layer perceptron (MLP) with two hidden layers that maps the feature representations to a space where a contrastive loss is applied. During training, the feature representations  $z_i, z_j$ , corresponding to two ‘correlated’ (differentially augmented) views of the same tile, are used to minimize the normalized temperature-scaled cross entropy (NT-Xent) defined as

$$l_{ij} = -\log \frac{\exp(\text{sim}(z_i, z_j)/\tau)}{\sum_{k=1}^N \mathbb{1}_{[k \neq i]} \exp(\text{sim}(z_i, z_k)/\tau)}, \quad (1)$$

where  $\text{sim}(\cdot)$  denotes cosine similarity,  $\tau$  is ‘temperature’, and  $\mathbb{1}_{[k \neq i]} \in \{0, 1\}$  is an indicator function evaluating to 1 iff  $k \neq i$ .

The trained ResNet-50 network is used as the base encoder to produce a set of hidden representations  $H = \{h_1, \dots, h_i, \dots, h_N\}$ ,  $h_i \in \mathbb{R}^{n \times d}$  of each WSI, where  $n$  is the number of tiles and  $d$  is the embedding dimension to represent each tile.

### 3.2 Neighbor-constrained attention module

To aggregate the feature embeddings  $H = \{h_1, \dots, h_i, \dots, h_N\}$ ,  $h_i \in \mathbb{R}^{n \times d}$ , where  $d$  is the embedding dimensions of a tile,  $n$  the number of tiles within a WSI, and  $N$  the number of WSIs - we use a transformer,  $T$ , layer to encode the feature embeddings of the individual tiles.

However, working with large WSIs can lead to memory overload, as the self-attention mechanism used in the transformer layer requires computing pairwise interactions between all of the tiles in each WSI. To circumvent the memory overload associated with the long-range dependencies of large WSIs we adopt the Nystromformer architecture [34] to model feature interactions that otherwise would be intractable.

The Nystromformer approach is based on the Nystrom method, which is a technique for approximating a kernel matrix by selecting a small subset of its rows and columns. In the context of the transformer layer, this means selecting a subset of "landmark" tiles from each WSI to represent the full set of tiles. The landmark tiles are chosen randomly, and their embeddings are used to compute a low-rank approximation of the self-attention matrix. This approximation is then used instead of the full self-attention matrix to compute the final output of the transformer layer.

The Nystromformer architecture is highly scalable with respect to sequence length, which makes it well-suited for processing large WSIs [34]. Additionally, by reducing the time complexity of the self-attention mechanism from  $\mathcal{O}(n^2)$  to  $\mathcal{O}(n)$ , the Nystromformer approach can significantly reduce the computational cost of processing each WSI. The approximate self-attention mechanism can be defined as follows:

$$t = \text{softmax}\left(\frac{Q_1 \tilde{K}_1^T}{\sqrt{d_k}}\right) \left(A\right)^+ \text{softmax}\left(\frac{\tilde{Q}_1 K_1^T}{\sqrt{d_k}}\right) V$$

where  $\tilde{Q}_1$  and  $\tilde{K}_1$  are the  $m$  selected landmarks from the original  $n$ -dimensional sequence of  $Q_1$  and  $K_1$ ,  $A^+ = \text{softmax}\left(\frac{\tilde{Q}_1 \tilde{K}_1^T}{\sqrt{d_k}}\right)^+$  is the approximate inverse of  $A$ , and  $\text{softmax}$  is applied along the rows of the matrix.

Given the tile-level hidden representations  $T = \{t_1, \dots, t_i, \dots, t_N\}$ , the neighbor-constrained attention network captures the interactions between the  $k$  spatially adjacent neighbors of every tile. First, the tile representations  $t_i$  are transformed by the weight matrices  $W^q \in \mathbb{R}^{n \times d_q}$ ,  $W^k \in \mathbb{R}^{n \times d_k}$  and  $W^v \in \mathbb{R}^{n \times d_v}$  into three distinct representations: the query representation  $Q(t_i) = W_q^T t_i$ , the key representation  $K(t_i) = W_k^T t_i$  and the value representation  $V(t_i) = W_v^T t_i$ , where  $d_q = d_k = d_v = d$ . The dot product of every query with all the key vectors produces an attention matrix whose elements determine the correlation between the different tiles of a WSI (Fig. 1).

The projection head of the trained SimCLR network is then used to transform the original  $t_i, t_j$  feature representations to a lower dimensional representation  $z_i \in R_d$ , where the distance is calculated.

$$\delta(z_i, z_j) = \sqrt{\sum_{i=1}^n (z_i - z_j)^2} \quad (2)$$

Subsequently, to prevent the attention network from attending to all tiles in a given WSI and constraining every tile to its nearest neighbors, we use the similarity mask:

$$s_{ij} = \begin{cases} \exp(-\delta_{ij}), & \text{if } j \in k\text{NN}(i) \\ 0, & \text{otherwise,} \end{cases} \quad (3)$$

where  $k\text{NN}(i)$  refers to the  $k$  spatially nearest neighbors to the patch  $i$  and  $\delta$  is the distance learnt by the SimCLR. This design ensures injecting a biological prior such that the weight of a tile is dependent on adjacent tiles with a similar pattern.

This mask is element-wise multiplied with the dot product of the query and key embeddings, generating a masked attention matrix whose non-zero elements reflect the contribution of a tile's neighbors to the tile score.

After obtaining the attention coefficients that correspond to the neighbors of every tile, the last step is to aggregate this contextual information to generate a single attention weight. For each tile, we sum the coefficients of their neighbors. The resultant tile score vector is passed through a softmax function to ensure that all weights sum to one.

Therefore, the attention coefficient of the  $i$ th tile of a WSI is given by the following equation, where  $\langle \cdot \rangle$  denotes the inner product between two vectors:

$$w_i = \frac{\exp \left( \sum_{j=1}^N \langle Q(t_i), K(t_j) \rangle s_{ij} \right)}{\sum_{k=1}^N \exp \left( \sum_{j=1}^n \langle Q(t_k), K(t_j) \rangle s_{kj} \right)}. \quad (4)$$

The feature embeddings  $t \in \mathbb{R}^{1 \times d_v}$  are then computed and weighted by their respective attention score to give a neighbor-constrained feature vector,  $g_i$ , for each tile:

$$g_i = w_i V(t_i). \quad (5)$$

### 3.3 Feature aggregation and slide-level prediction

The collective, WSI-level representation  $g \in \mathbb{R}^{1 \times d}$  is adaptively computed as the average of the value vectors weighted by their respective attention score:

$$g = \sum_{i=1}^N a_i (g_i + t_i), \quad (6)$$

such that:

$$a_i = \frac{\exp w^T (\tanh(Vt_i^T) \odot \text{sigm}(Ut_i^T))}{\sum_{j=1}^K \exp w^T (\tanh(Vt_j^T) \odot \text{sigm}(Ut_j^T))}, \quad (7)$$

where  $U, V, w$  are learnable parameters,  $\odot$  is an element-wise multiplication,  $\text{sigm}()$  is the sigmoid non-linearity and  $\tanh()$  the hyperbolic tangent function.

Finally, the slide-level score is given via the classifier layer  $W_c \in \mathbb{R}^{c \times d}$ :

$$y_{\text{slide}} = W_c g^T, \quad (8)$$

where  $c$  corresponds to the number of classes. The representation obtained from the high-attended patches is used to minimise a cross-entropy loss, and a final classification score is produced.

## 4 Experiments

We sought to determine if CAMIL can effectively capture informative neighbor relationships and, if so, determine whether neighbor relationships can improve MIL performance. To this end, we evaluated CAMIL on two histopathology datasets. This section includes our experimental setup, an overview of our baselines as well as a result on test data.

### 4.0.1 Datasets

We conducted a series of experiments in two publicly available and widely-used datasets of WSIs: the Camelyon16 and TCGA-NSCLC datasets.

Camelyon16 [35] is one of the largest publicly available breast cancer datasets. It consists of a training set of 270 annotated biopsy slides and an official test set of 129 slides collected at the Radboud University Medical Center and the University Medical Center Utrecht in the Netherlands.

The TCGA-NSCLC dataset includes two non-small cell lung cancer subtypes: Lung Squamous Cell Carcinoma (TCGA-LUSC) and Lung Adenocarcinoma (TCGA-LUAD). There are 541 LUAD slides from 478 cases and 512 LUSC slides from 478 cases.

#### 4.0.2 Experimental Settings

In the case of Camelyon16, the WSIs are partitioned into a training and test set. The 270 WSIs of the training set are split five times into a training (80%) and a validation (20%) set in a 5-fold cross-validation fashion, and the average performance of the model on the competition test set is reported. The official test set comprised of 129 WSIs is used for evaluation. Regarding the TCGA-NSCLC, after ensuring that different slides from the same patient are not distributed in both the training and test sets, a 4-fold cross-validation with a ratio of training:validation:test=60:15:25 is used.

#### 4.0.3 Baselines

We evaluated the performance of our neighbor pooling strategy by comparing it to traditional pooling operators such as Mean-pooling and Max-pooling and other state-of-the-art MIL methods, including AB-MIL [36], CLAM-SB, CLAM-MB [21], MI Net, MIL-RNN [17], TransMIL [37], and DTFT-MIL [28]. AB-MIL implements attention based on the features of each individual tile, while CLAM-SB and CLAM-MB use the same attention pooling operator as AB-MIL but are supported by an auxiliary clustering layer. MI Net uses max pooling and mean pooling to derive the WSI-level embedding, while MIL-RNN is a recurrent neural network-based aggregation model. TRANS-MIL is a transformer-based aggregator operator, and DTFT-MIL uses the class activation map to derive the positive probability of an instance under the AB-MIL framework.

#### 4.0.4 Implementation Details

Using the publicly available WSI-preprocessing toolbox developed by [21], we first automatically segmented the tissue region from each slide and exhaustively divided it into  $256 \times 256$  non-overlapping patches using  $\times 20$  magnification (Fig. 1). It is important to note that using different parameters in the feature extraction process can lead to different training and test sets, which can subsequently result in different model performance. To ensure the reproducibility of our results, we provide the features that we used in our study. By sharing the extracted features, other researchers can use the same data to train and test their models, making it easier to compare different approaches. This also allows for the replication and validation of our results, which is a crucial aspect of scientific research.

For the SimCLR component in our pipeline, a stochastic data augmentation module was deployed, enabling four types of augmentations: color distortion, rotation, zoom and vertical flip. Our SimCLR network consists of a feature extractor, a pre-trained ResNet50 network that compressed each augmented tile to a 1024-dimensional feature representation followed by a projection head, which is an MLP with two hidden layers. The projection head further transformed every feature vector into a 512-dimensional representation. The model whose parameters were updated via the Adam optimizer with an L2 weight decay of  $1e-5$  and a learning rate of 0.004 minimizes normalized temperature-scaled cross-entropy. For the definition of the nearest neighbors in Equation 3, we first compute the Euclidean distances between all the tiles of a WSI. Then, for any given tile, we considered as nearest neighbors up to the ten spatially closest tiles.

Minimization of the cross-entropy loss was achieved via stochastic gradient descent (SGD) using the Adam optimizer [38] with a learning rate of 0.0002 and weight decay of  $1e-5$ . All the models were trained for a maximum of 100 epochs if the early stopping criterion, utilized to avoid overfitting, was not met. The saved model with the lowest validation loss was then tested on the test set.

## 5 Results

The results of using CAMIL to classify WSI in the Camelyon16 and TCGA-NSCLC datasets are presented in Tables 1–2. For all the experiments, the area under the receiver operating characteristic curve (AUC), the slide-level accuracy (ACC), which is determined by the threshold of 0.5, and the macro-averaged  $F_1$  score are considered. These procedures enabled a fair comparison between the different approaches across differently sized datasets [39]. Note that the reported results are computed without a search for optimal setup.

On the Camelyon16 cancer dataset, CAMIL outperformed all the existing MIL models regarding accuracy and AUC. Importantly, in the Camelyon16 dataset, tumor cells may account for as little as 5% of any WSI. The low frequency of tumor cells in tissue samples is particularly common [40] to metastatic sites, where tumor cells are interspersed within large regions of normal cells. Thus CAMIL - which re-adjusts the attention coefficients by inspecting a tile’s small neighborhood - was more effective at identifying clinically relevant, sparse, cancerous regions than other models. Indeed, CAMIL outperformed the other baselines on the Camelyon16 dataset by significant margins. CAMIL is at least 1.5% better in AUC than other existing models.

METHOD	ACC( $\uparrow$ )	$F_1$ ( $\uparrow$ )	AUC( $\uparrow$ )
MEAN-POOLING	0.717 $\pm$ 0.015	0.640 $\pm$ 0.022	0.620 $\pm$ 0.017
MAX-POOLING	0.829 $\pm$ 0.012	0.797 $\pm$ 0.019	0.827 $\pm$ 0.021
ABMIL-GATED	0.844 $\pm$ 0.021	0.822 $\pm$ 0.027	0.851 $\pm$ 0.004
MIL-RNN	0.849 $\pm$ 0.023	0.831 $\pm$ 0.031	0.857 $\pm$ 0.004
CLAM-SB	0.851 $\pm$ 0.009	0.831 $\pm$ 0.011	0.876 $\pm$ 0.017
CLAM-MB	0.860 $\pm$ 0.026	0.842 $\pm$ 0.027	0.904 $\pm$ 0.028
TRANSMIL	0.836 $\pm$ 0.024	0.816 $\pm$ 0.023	0.845 $\pm$ 0.029
DTFT-MIL	0.855 $\pm$ 0.029	0.809 $\pm$ 0.032	0.904 $\pm$ 0.009
CAMIL	<b>0.869</b> $\pm$ 0.013	<b>0.860</b> $\pm$ 0.017	0.920 $\pm$ 0.027

Table 1: Performance comparison of CAMIL against various baselines on the CAMELYON16 cancer dataset comprising of H&E stained images. The best-performing results are highlighted in bold.

METHOD	ACC( $\uparrow$ )	$F_1$ ( $\uparrow$ )	AUC( $\uparrow$ )
MEAN-POOLING	0.858 $\pm$ 0.026	0.858 $\pm$ 0.027	0.927 $\pm$ 0.017
MAX-POOLING	0.864 $\pm$ 0.011	0.864 $\pm$ 0.010	0.937 $\pm$ 0.009
ABMIL-GATED	0.846 $\pm$ 0.008	0.845 $\pm$ 0.008	0.925 $\pm$ 0.022
MIL-RNN	0.853 $\pm$ 0.022	0.850 $\pm$ 0.022	0.918 $\pm$ 0.022
CLAM-SB	0.847 $\pm$ 0.027	0.848 $\pm$ 0.027	0.919 $\pm$ 0.027
CLAM-MB	0.839 $\pm$ 0.023	0.839 $\pm$ 0.023	0.920 $\pm$ 0.007
TRANSMIL	0.865 $\pm$ 0.013	0.863 $\pm$ 0.013	0.923 $\pm$ 0.014
DTFT-MIL	0.860 $\pm$ 0.008	0.856 $\pm$ 0.012	0.926 $\pm$ 0.014
CAMIL	<b>0.871</b> $\pm$ 0.001	<b>0.879</b> $\pm$ 0.0013	<b>0.945</b> $\pm$ 0.0018

Table 2: Performance comparison of CAMIL against various baselines on the TCGA-NSCLC dataset comprising of H&E stained images. The best-performing results are highlighted in bold.

In the TCGA-NSCLC dataset, CAMIL outperformed all the other considered baselines. Notably, the comparably simple max-pooling method, which uses the max operator as an aggregation function, was among the best-performing models. The unexpected effectiveness of max-pooling on this dataset likely stems from the fact that in the TCGA-NSCLC dataset, tumor cells typically make up around 80% of the WSI. Thus the probability that individual cancerous tiles are correctly labelled is high.

In addition to the quantitative results, we also performed a qualitative evaluation of our method by visualizing the attention maps of different methods on expertly annotated tumor regions. These attention maps can pinpoint diagnostically significant locations in the image that are crucial for accurate tumor identification. CAMIL makes use of the un-normalized attention scores. Due to the local similarity mask, the attention weights of similar neighboring feature representations are accumulated and provide strong activations. As such, the non-cancerous regions are characterized by negative activations, whereas the tumor regions are by positive ones, as illustrated in Fig. 7. By filtering out the negative attention scores and dissociating the score of each tile from that of another, CAMIL can accurately recognize the low-strength signal of non-cancerous regions, similar to the DTFT-MIL model. After filtering out attention scores lower than 0.5, the remaining attention scores were binarized for presentation purposes and mapped to their location in the WSI (with green color). The attention maps shown in Fig. 3 suggest that CAMIL is more effective at accurately detecting regions of attention in cancerous images compared to other models, such as DTFT-MIL and AB-MIL. This is because CAMIL takes into account the co-dependencies that exist between different instances by leveraging the idiosyncrasies of each tile’s neighborhood. This allows the model to produce attention maps that are more consistent with fewer tiles sparsely distributed within a whole slide image (WSI). In contrast, DTFT-MIL and AB-MIL rely on the independence assumption, neglecting these co-dependencies and resulting in the detection of positive instances that appear rather scarce and dispersed.

Fig. 4 provides a second visual example of the attention maps generated by CAMIL, DTFT-MIL, and classic AB-MIL models on the Camelyon16 cancer dataset. The attention maps in Fig. 4 show that CAMIL achieved high predictive performance and could accurately determine the boundaries between normal and tumor tissue. It also performed better than the other models in identifying the edge regions of tumors. In contrast, the AB-MIL model tended to assign significant importance to sparse tissue areas surrounding major tissues, as it benefits from choosing these neutral regions to represent negative slides, as opposed to non-tumor tissue regions. DTFT-MIL, on the other hand, did not exhibit this behavior, as the derived probabilities were explicitly relevant to the class estimations of the trained model. However,



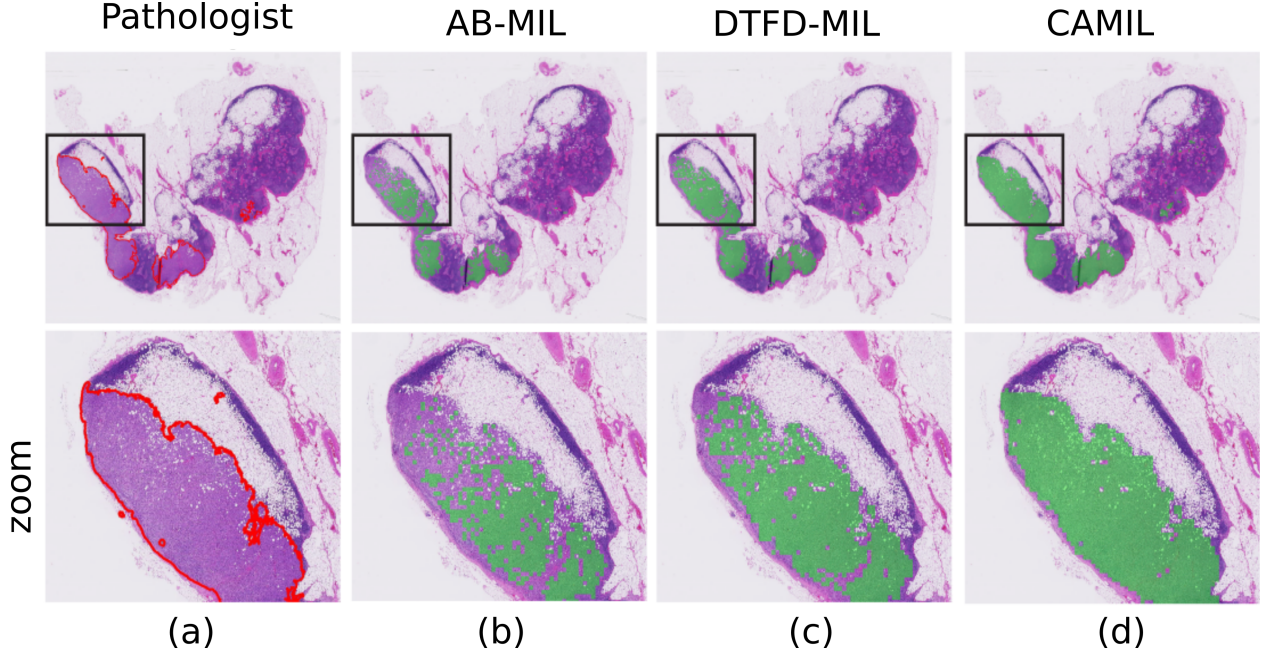


Figure 3: A visual example of the tumor regions and attention maps produced by different models on the Camelyon16 cancer dataset. The top row shows the whole slide image, and the bottom row shows the zoomed-in area within the black box. (a) Shows the pathologists ground truth annotations with tumor regions delineated by red lines. (b-d) Shows the attention maps for AB-MIL, DTFD-MIL, and CAMIL, respectively, pinpointing diagnostically significant locations on the Camelyon16 cancer dataset. In classic AB-MIL, the attention scores were normalized as  $a'_k = \frac{a_k - a_{\min}}{a_{\max} - a_{\min}}$ , while in the case of DTFT-MIL scores are calculated directly from the patch probability derivation.

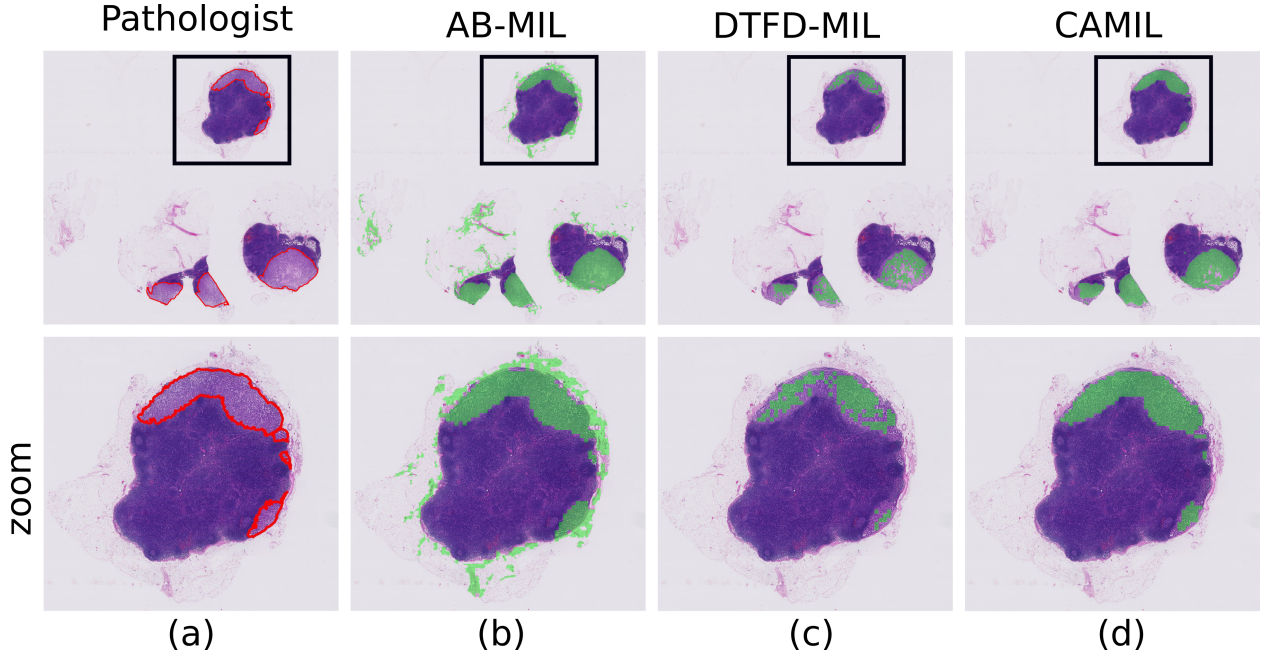


Figure 4: A visual example of the sparse-tissue tumor regions and attention maps produced by different models on the Camelyon16 cancer dataset. Similar to Fig. 3 above, (a) shows the ground truth annotations, with (b-d) showing the attention maps of AB-MIL, DTFD-MIL, and CAMIL, respectively.

its attention maps were less cohesive, with scattered patches of high importance in certain areas, particularly near the tumour's edges.

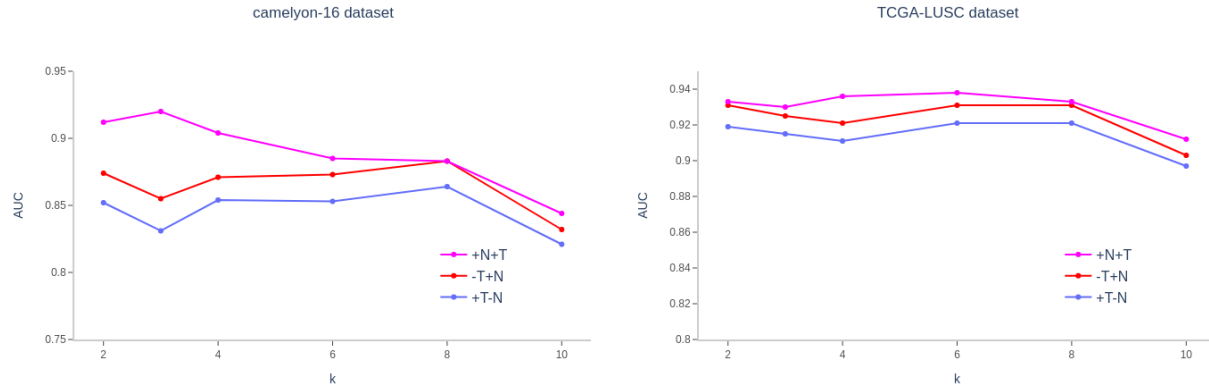


Figure 5: The relationship between the hyperparameter “ $k$ ” and the corresponding AUC values for Camelyon16 and TCGA-NSCLC histopathology datasets.

## 6 Ablation studies

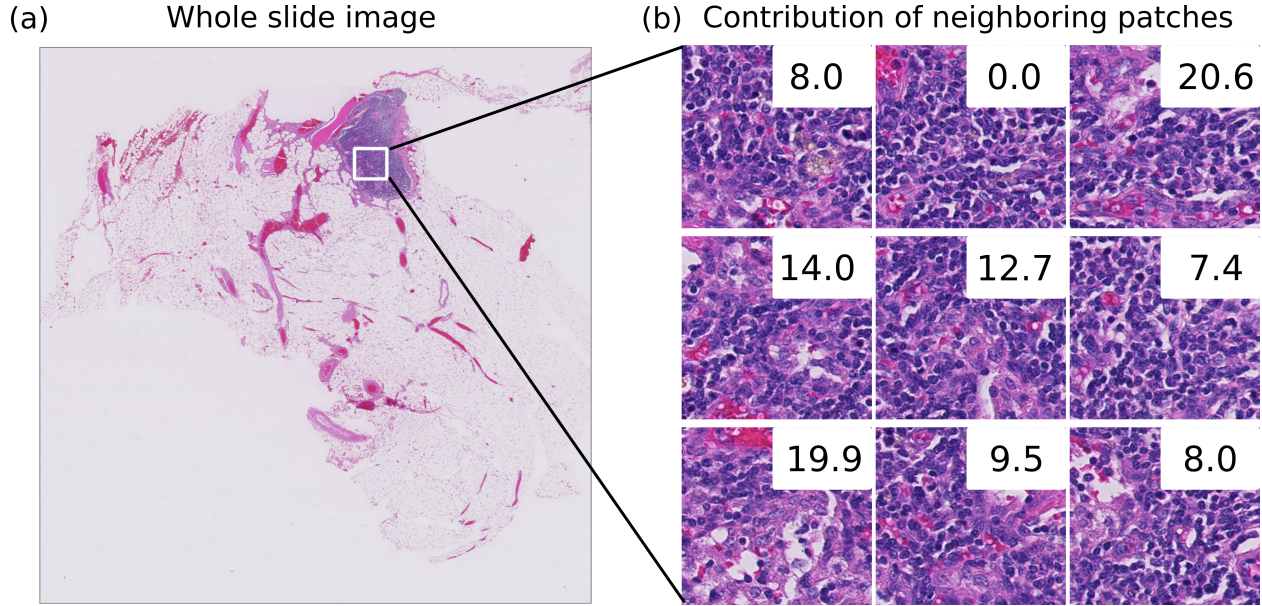


Figure 6: Assigning weights of neighboring patches based on similarity scores. (a) Shows a WSI from the Camelyon16 dataset. (b) Shows an example of how the neighboring attention mechanisms help identify the most important regions of the WSI for making a classification decision, ultimately leading to more accurate and reliable results.

We conducted experiments to investigate the impact of the number of neighbors, denoted as  $k$ , on the performance of our model CAMIL (purple line in Fig. 5). By varying  $k$  and training the model under the same experimental conditions, we found that for small values of  $k$  (i.e.,  $k \in \{2, 3, 4\}$ ), the model performed similarly, which is reasonable since neighboring tiles provide the most relevant information about the probability of a tile being cancerous. This robustness in the choice of  $k$  is desirable since hyperparameter tuning can be time-consuming. However, as  $k$  increased, the model’s performance gradually decreased, except for when  $k = 8$ , where the performance improved again. This could be explained by the formation of patterns in tumors that repeat approximately every eight tiles, highlighting the importance of models that can capture both local neighboring information and overall patterns in the biopsy. We also observed that selecting either  $k = 4$  or  $k = 8$  consistently produced satisfactory results due to the spatial arrangement of tiles and their neighbors, which resembles a grid-like topology. With  $k = 4$ , the tiles are considered neighboring if they are 1-connected, and with  $k = 8$ , they are considered neighboring if they are 2-connected, offering an increased field-of-view (FOV) for the central tile.



## Attention distribution of tiles from normal and tumour slides

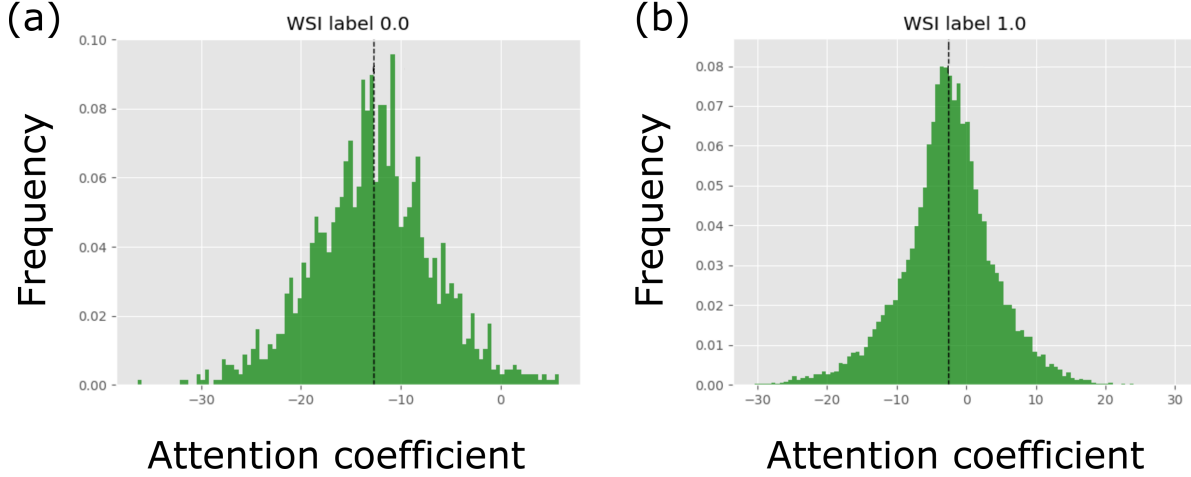


Figure 7: Attention distribution of a normal and cancerous slide. The dashed line indicates the mean.

Additionally, our ablation study aimed to investigate the effectiveness of the Nystromformer block and the neighboring attention module. Specifically, we examined the impact of varying the number of neighbors in the Nystromformer block and excluding it altogether while keeping the attention module. The results showed (blue line in Fig. 5) that using only the Nystromformer block did not lead to satisfactory performance, indicating that the neighboring attention module is crucial for achieving improved outcomes. Moreover, when we removed the Nystromformer block and retained the attention module (red line in Fig. 5), the model performed better, indicating that the attention module is sufficient for this task.

Following our expectations, with or without the use of the SimCLR model, the Camelyon16 dataset is more sensitive to the  $k$  hyperparameter as opposed to the TCGA dataset. This is attributed to the nature of the Camelyon16 dataset. Here, the tumor regions are highly localized, accounting for less than 5% of the entire WSI. Thus, the use of a neighboring mask which is locality sensitive can elucidate different morphological evidence for every  $k$ .

We have provided an example of our neighbor-constrained-attention mechanism in Fig. 6. In this example, we have considered a tile’s eight closest neighbors and highlighted the contribution of each neighboring tile in the final attention score of the central tile using white letters. The central tile mostly comprises normal cells with a few scarce tumor cells visible on its bottom half. Without additional information, this tile could be assigned a lower attention score due to the scarcity of tumor cells. However, when we investigate its neighborhood, we can see that it is surrounded by some tumor tiles. The final attention coefficient of each tile is determined through a neighbor-constrained-attention mechanism, which incorporates two criteria. The first criterion is morphological similarity, obtained through a similarity mask. The second criterion is an attention coefficient produced by the dot product of the keys and query vector. Tiles that exhibit high morphological similarity and strong activations are given greater weight in the final attention coefficient calculation, while tiles with low similarity and poor activations are less impactful and thus contribute less. This approach ensures that the central tile is accurately represented in the final attention score while simultaneously allowing the attention mechanism to focus on the most relevant features in the neighboring tiles.

## 7 Conclusion

Current DNN models use attention mechanisms to accurately diagnose cancer and precisely pinpoint the location of cancer evidence in a WSI. Those attention mechanisms are based either on MIL attention or self-attention pooling. The first aggregation rule generates an attention score for every tile on the image based on the independence assumption, while the latter uses vision transformers to generate an attention score that captures the correlation among different tiles.

We have presented CAMIL, a novel MIL vision transformer-based approach that takes into account the dependencies of neighboring tiles in a histopathology image in an effort to re-adjust the calculated attention scores based on the similarities they share. CAMIL offers both interpretability and performance gains, and aims at easing pathologists’ workload and increasing the amount of available data by exploiting the slide-level labels.

## Acknowledgment

This study represents independent research funded by the National Institute for Health Research (NIHR) Biomedical Research Centre at The Royal Marsden NHS Foundation Trust and the Institute of Cancer Research, London. The views expressed are those of the author(s) and not necessarily those of the NIHR or the Department of Health and Social Care.

## References

- [1] Guy B. Faguet. A brief history of cancer: Age-old milestones underlying our current knowledge database. *International Journal of Cancer*, 136(9):2022–2036, 2015.
- [2] Sandra Morales, Kjersti Engan, and Valery Naranjo. Artificial intelligence in computational pathology - challenges and future directions. *Digit. Signal Process.*, 119:103196, 2021.
- [3] Kausik Das, Sailesh Conjeti, Abhijit Guha Roy, Jyotirmoy Chatterjee, and Debdoot Sheet. Multiple instance learning of deep convolutional neural networks for breast histopathology whole slide classification. In *15th IEEE International Symposium on Biomedical Imaging, ISBI 2018, Washington, DC, USA, April 4-7, 2018*, pages 578–581. IEEE, 2018.
- [4] Gwénolé Quéllec, Mathieu Lamard, Michel Cozic, Gouenou Coatrieux, and Guy Cazuguel. Multiple-instance learning for anomaly detection in digital mammography. *IEEE Trans. Medical Imaging*, 35(7):1604–1614, 2016.
- [5] Tong Tong, Robin Wolz, Qinquan Gao, Ricardo Guerrero, Joseph V. Hajnal, and Daniel Rueckert. Multiple instance learning for classification of dementia in brain MRI. *Medical Image Anal.*, 18(5):808–818, 2014.
- [6] Jaime Melendez, Bram van Ginneken, Pragnya Maduskar, Rick H. H. M. Philipsen, Klaus Reither, Marianne Breuninger, Ifedayo M. O. Adetifa, Rahmatulai Maane, Helen Ayles, and Clara I. Sánchez. A novel multiple-instance learning-based approach to computer-aided detection of tuberculosis on chest x-rays. *IEEE Trans. Medical Imaging*, 34(1):179–192, 2015.
- [7] Chetan L. Srinidhi, Ozan Ciga, and Anne L. Martel. Deep neural network models for computational histopathology: A survey. *CoRR*, abs/1912.12378, 2019.
- [8] Xiaodong Wang, Ying Chen, Yunshu Gao, Huiqing Zhang, Zehui Guan, Zhou Dong, Yuxuan Zheng, Jiarui Jiang, Haoqing Yang, Liming Wang, Xianming Huang, Lirong Ai, Wenlong Yu, Hongwei Li, Changsheng Dong, Zhou Zhou, Xiyang Liu, and Guanzhen Yu. Predicting gastric cancer outcome from resected lymph node histopathology images using deep learning. *Nature Communications*, 12(1):1637, March 2021. Number: 1 Publisher: Nature Publishing Group.
- [9] Yan Xu, Jun-Yan Zhu, Eric I-Chao Chang, Maode Lai, and Zhuowen Tu. Weakly supervised histopathology cancer image segmentation and classification. *Medical Image Anal.*, 18(3):591–604, 2014.
- [10] Pierre Courtiol, Eric W. Tramel, Marc Sanselme, and Gilles Wainrib. Classification and disease localization in histopathology using only global labels: A weakly-supervised approach. *CoRR*, abs/1802.02212, 2018.
- [11] Gang Xu, Zhigang Song, Zhuo Sun, Calvin Ku, Zhe Yang, Cancheng Liu, Shuhao Wang, Jianpeng Ma, and Wei Xu. CAMEL: A weakly supervised learning framework for histopathology image segmentation. In *2019 IEEE/CVF International Conference on Computer Vision, ICCV 2019, Seoul, Korea (South), October 27 - November 2, 2019*, pages 10681–10690, 2019.
- [12] Changjiang Zhou, Yi Jin, Yuzong Chen, Shan Huang, Rengpeng Huang, Yuhong Wang, Youcai Zhao, Yao Chen, Lingchuan Guo, and Jun Liao. Histopathology classification and localization of colorectal cancer using global labels by weakly supervised deep learning. *Comput. Medical Imaging Graph.*, 88:101861, 2021.
- [13] Yash Sharma, Aman Shrivastava, Lubaina Ehsan, Christopher A. Moskaluk, Sana Syed, and Donald E. Brown. Cluster-to-conquer: A framework for end-to-end multi-instance learning for whole slide image classification. In Mattias P. Heinrich, Qi Dou, Marleen de Bruijne, Jan Leilmann, Alexander Schlaefel, and Floris Ernst, editors, *Medical Imaging with Deep Learning, 7-9 July 2021, Lübeck, Germany*, volume 143 of *Proceedings of Machine Learning Research*, pages 682–698. PMLR, 2021.
- [14] Chensu Xie, Hassan Muhammad, Chad M. Vanderbilt, Raul Caso, Dig Vijay Kumar Yarlagadda, Gabriele Campanella, and Thomas J. Fuchs. Beyond classification: Whole slide tissue histopathology analysis by end-to-end part learning. In Tal Arbel, Ismail Ben Ayed, Marleen de Bruijne, Maxime Descoteaux, Hervé Lombaert, and Christopher Pal, editors, *International Conference on Medical Imaging with Deep Learning, MIDL 2020, 6-8 July 2020, Montréal, QC, Canada*, volume 121 of *Proceedings of Machine Learning Research*, pages 843–856, 2020.

- [15] Zhuchen Shao, Hao Bian, Yang Chen, Yifeng Wang, Jian Zhang, Xiangyang Ji, and Yongbing Zhang. Transmil: Transformer based correlated multiple instance learning for whole slide image classification. In Marc’Aurelio Ranzato, Alina Beygelzimer, Yann N. Dauphin, Percy Liang, and Jennifer Wortman Vaughan, editors, *Advances in Neural Information Processing Systems 34: Annual Conference on Neural Information Processing Systems 2021, NeurIPS 2021, December 6-14, 2021, virtual*, pages 2136–2147, 2021.
- [16] Ming Tu, Jing Huang, Xiaodong He, and Bowen Zhou. Multiple instance learning with graph neural networks. *CoRR*, abs/1906.04881, 2019.
- [17] Gabriele Campanella, Matthew G. Hanna, Luke Geneslaw, Allen P. Miraflor, Vitor Werneck Krauss Silva, Klaus J. Busam, Edi Brogi, Victor E. Reuter, David S. Klimstra, and Thomas J. Fuchs. Clinical-grade computational pathology using weakly supervised deep learning on whole slide images. *Nature Medicine*, pages 1–9, 2019.
- [18] Gabriel Landini, Giovanni Martinelli, and Filippo Piccinini. Colour deconvolution: stain unmixing in histological imaging. *Bioinformatics*, 09 2020. btaa847.
- [19] Le Hou, Dimitris Samaras, Tahsin M. Kurç, Yi Gao, James E. Davis, and Joel H. Saltz. Patch-based convolutional neural network for whole slide tissue image classification. In *2016 IEEE Conference on Computer Vision and Pattern Recognition, CVPR 2016, Las Vegas, NV, USA, June 27-30, 2016*, pages 2424–2433. IEEE Computer Society, 2016.
- [20] Maximilian Ilse, Jakub M. Tomczak, and Max Welling. Attention-based deep multiple instance learning. In Jennifer G. Dy and Andreas Krause, editors, *Proceedings of the 35th International Conference on Machine Learning, ICML 2018, Stockholmsmässan, Stockholm, Sweden, July 10-15, 2018*, volume 80 of *Proceedings of Machine Learning Research*, pages 2132–2141, 2018.
- [21] Ming Y Lu, Drew FK Williamson, Tiffany Y Chen, Richard J Chen, Matteo Barbieri, and Faisal Mahmood. Data-efficient and weakly supervised computational pathology on whole-slide images. *Nature Biomedical Engineering*, 5(6):555–570, 2021.
- [22] Xinggong Wang, Yongluan Yan, Peng Tang, Xiang Bai, and Wenyu Liu. Revisiting multiple instance neural networks. *Pattern Recognit.*, 74:15–24, 2018.
- [23] Ashish Vaswani, Noam Shazeer, Niki Parmar, Jakob Uszkoreit, Llion Jones, Aidan N. Gomez, Lukasz Kaiser, and Illia Polosukhin. Attention is all you need. In Isabelle Guyon, Ulrike von Luxburg, Samy Bengio, Hanna M. Wallach, Rob Fergus, S. V. N. Vishwanathan, and Roman Garnett, editors, *Advances in Neural Information Processing Systems 30: Annual Conference on Neural Information Processing Systems 2017, December 4-9, 2017, Long Beach, CA, USA*, pages 5998–6008, 2017.
- [24] Jingwei Zhang, Ke Ma, John S. Van Arnam, Rajarsi Gupta, Joel H. Saltz, Maria Vakalopoulou, and Dimitris Samaras. A joint spatial and magnification based attention framework for large scale histopathology classification. In *IEEE Conference on Computer Vision and Pattern Recognition Workshops, CVPR Workshops 2021, virtual, June 19-25, 2021*, pages 3776–3784. Computer Vision Foundation / IEEE, 2021.
- [25] Aïcha BenTaieb and Ghassan Hamarneh. Predicting cancer with a recurrent visual attention model for histopathology images. In Alejandro F. Frangi, Julia A. Schnabel, Christos Davatzikos, Carlos Alberola-López, and Gabor Fichtinger, editors, *Medical Image Computing and Computer Assisted Intervention - MICCAI 2018 - 21st International Conference, Granada, Spain, September 16-20, 2018, Proceedings, Part II*, volume 11071 of *Lecture Notes in Computer Science*, pages 129–137. Springer, 2018.
- [26] Jiayun Li, Wenyuan Li, Anthony E. Sisk, Huihui Ye, W. Dean Wallace, William Speier, and Corey W. Arnold. A multi-resolution model for histopathology image classification and localization with multiple instance learning. *Comput. Biol. Medicine*, 131:104253, 2021.
- [27] Jiawen Yao, Xinliang Zhu, Jitendra Jonnagaddala, Nicholas J. Hawkins, and Junzhou Huang. Whole slide images based cancer survival prediction using attention guided deep multiple instance learning networks. *Medical Image Anal.*, 65:101789, 2020.
- [28] Hongrun Zhang, Yanda Meng, Yitian Zhao, Yihong Qiao, Xiaoyun Yang, Sarah E. Coupland, and Yalin Zheng. DTFD-MIL: double-tier feature distillation multiple instance learning for histopathology whole slide image classification. In *IEEE/CVF Conference on Computer Vision and Pattern Recognition, CVPR 2022, New Orleans, LA, USA, June 18-24, 2022*, pages 18780–18790, 2022.
- [29] David Tellez, Geert Litjens, Jeroen van der Laak, and Francesco Ciompi. Neural image compression for gigapixel histopathology image analysis. *IEEE Trans. Pattern Anal. Mach. Intell.*, 43(2):567–578, 2021.
- [30] Mohammed Adnan, Shivam Kalra, and Hamid R. Tizhoosh. Representation learning of histopathology images using graph neural networks. In *2020 IEEE/CVF Conference on Computer Vision and Pattern Recognition, CVPR Workshops 2020, Seattle, WA, USA, June 14-19, 2020*, pages 4254–4261. Computer Vision Foundation / IEEE, 2020.

- [31] Bin Li, Yin Li, and Kevin W. Eliceiri. Dual-stream multiple instance learning network for whole slide image classification with self-supervised contrastive learning. *CoRR*, abs/2011.08939, 2020.
- [32] Yu Zhao, Fan Yang, Yuqi Fang, Hailing Liu, Niyun Zhou, Jun Zhang, Jiarui Sun, Sen Yang, Bjoern H. Menze, Xinjuan Fan, and Jianhua Yao. Predicting lymph node metastasis using histopathological images based on multiple instance learning with deep graph convolution. In *2020 IEEE/CVF Conference on Computer Vision and Pattern Recognition, CVPR 2020, Seattle, WA, USA, June 13-19, 2020*, pages 4836–4845. Computer Vision Foundation / IEEE.
- [33] Ting Chen, Simon Kornblith, Mohammad Norouzi, and Geoffrey E. Hinton. A simple framework for contrastive learning of visual representations. In *Proceedings of the 37th International Conference on Machine Learning, ICML 2020, 13-18 July 2020, Virtual Event*, volume 119 of *Proceedings of Machine Learning Research*, pages 1597–1607. PMLR, 2020.
- [34] Yunyang Xiong, Zhanpeng Zeng, Rudrasis Chakraborty, Mingxing Tan, Glenn Fung, Yin Li, and Vikas Singh. Nyströmformer: A nyström-based algorithm for approximating self-attention. In *Thirty-Fifth AAAI Conference on Artificial Intelligence, AAAI 2021, Thirty-Third Conference on Innovative Applications of Artificial Intelligence, IAAI 2021, The Eleventh Symposium on Educational Advances in Artificial Intelligence, EAAI 2021, Virtual Event, February 2-9, 2021*, pages 14138–14148. AAAI Press, 2021.
- [35] Babak Ehteshami Bejnordi, Mitko Veta, Paul Johannes van Diest, Bram van Ginneken, Nico Karssemeijer, Geert Litjens, Jeroen A. W. M. van der Laak, and and the CAMELYON16 Consortium. Diagnostic Assessment of Deep Learning Algorithms for Detection of Lymph Node Metastases in Women With Breast Cancer. *JAMA*, 318(22):2199–2210, December 2017.
- [36] A. Andersson, N. Koriakina, N. Sladoje, and J. Lindblad. End-to-end multiple instance learning with gradient accumulation. In *2022 IEEE International Conference on Big Data (Big Data)*, pages 2742–2746, Los Alamitos, CA, USA, dec 2022. IEEE Computer Society.
- [37] Zhuchen Shao, Hao Bian, Yang Chen, Yifeng Wang, Jian Zhang, Xiangyang Ji, and Yongbing Zhang. TransMIL: Transformer based correlated multiple instance learning for whole slide image classification. In A. Beygelzimer, Y. Dauphin, P. Liang, and J. Wortman Vaughan, editors, *Advances in Neural Information Processing Systems*, 2021.
- [38] Diederik P. Kingma and Jimmy Ba. Adam: A method for stochastic optimization. In Yoshua Bengio and Yann LeCun, editors, *ICLR (Poster)*, 2015.
- [39] Paul Tourniaire, Marius Ilie, Paul Hofman, Nicholas Ayache, and Hervé Delingette. MS-CLAM: mixed supervision for the classification and localization of tumors in whole slide images. *Medical Image Anal.*, 85:102763, 2023.
- [40] Jun Cheng, Yuting Liu, Wei Huang, Wenhui Hong, Lingling Wang, Xiaohui Zhan, Zhi Han, Dong Ni, Kun Huang, and Jie Zhang. Computational Image Analysis Identifies Histopathological Image Features Associated With Somatic Mutations and Patient Survival in Gastric Adenocarcinoma. *Frontiers in Oncology*, 11, 2021.